International Journal of Heat and Mass Transfer 245 (2025) 127035

Contents lists available at ScienceDirect

International Journal of Heat and Mass Transfer

journal homepage: www.elsevier.com/locate/ijhmt

A new mechanistic model for post-dryout heat transfer based on two-region approach

Zihan Xia *, Xu Cheng

Institute for Applied Thermofluidics (IATF), Karlsruhe Institute of Technology (KIT), Kaiserstrasse 12, 76131, Karlsruhe, Germany

ARTICLE INFO

Keywords:
Post-dryout heat transfer
Two-region model
Droplet evaporation
Droplet deposition

ABSTRACT

Considering the significant difference in droplet evaporation rates between the near-wall and central regions during post-dryout heat transfer, as well as the limitations of existing mechanistic models in addressing this discrepancy, this paper proposes a two-region model for interfacial heat transfer calculations. The proposed model divides the flow field into a central region and a near-wall region, performing separate calculations for droplet evaporation and droplet interactions in each region. The radial vapor temperature distribution is determined by fitting CFD results, which subsequently provides the near-wall vapor temperature profile necessary for interfacial heat transfer calculations. Additionally, a new droplet deposition model is developed to calculate the mass flow of droplets transferring between the central and near-wall regions. The proposed model is validated against experimental data obtained from Freon R-134a and water experiments. Evaluation results indicate that the model accurately predicts wall superheating and the heat transfer coefficient in the post-dryout region, thereby enhancing the predictive capability of mechanistic post-dryout heat transfer models.

1. Introduction

During the operation of heat exchange systems like thermal power plants and nuclear reactors, post-dryout may occur under various conditions. Fig. 1 illustrates the flow regime "annular flow", the dryout point and the post-dryout (PDO) region. In this case, the liquid film in the annular flow regime gradually thins and eventually evaporates all its mass due to continuous evaporation and liquid entrainment. The point where the liquid film completely disappears is known as the dryout point. The convective heat transfer mechanism abruptly shifts from boiling heat transfer to single-phase vapor convection heat transfer, leading to a sudden decrease in the heat transfer coefficient and a sharp increase in the wall temperature of the heated surface. The region beyond the dryout point is referred to as post-dryout (PDO) region, characterized by a dispersed flow pattern. Here, the liquid exits only in the form of droplets and no continuous liquid can cover the heated surface. Vapor conducts convective heat exchange with the heated surface and becomes superheated, represented by the progressively deepening red color in Fig. 1. The liquid droplets are dispersed in the superheated vapor at saturation temperature. Driven by the temperature difference between droplets and vapor, heat is transferred from the superheated vapor to droplets, which slows down the process of vapor superheating, thus affecting the developing trend of wall temperature after dryout. Reliable description of the heat transfer mechanism in the PDO region is critical for determining the maximum wall temperature of the heated surface, which is essential for evaluating whether the structural integrity of the heated surface in heat exchange systems can be maintained under various operating conditions.

Research on post-dryout heat transfer has been going on for >50 years. The research scope involves experimental and theoretical studies. Experimental research conducted by previous researchers [1–5] with different fluids encompasses a wide range of mass flux, heat flux, pressure and tube size. From the analysis of the experimental data, several correlations for predicting the wall temperature and heat transfer coefficient in PDO region have been developed by modifying the Dittus-Boelter correlation [6,7]. In these correlations [8–10] the vapor temperature is assumed to be the saturation temperature with the assumption that the vapor will not be superheated until all the droplets are evaporated. But soon, with the improvement of the experimental techniques, the vapor temperature in mist flow was measured. It was found that the vapor could be superheated even in the existence of large amount of droplets [11]. The discovery of thermal non-equilibrium demonstrates that the implementation of saturation vapor temperature for PDO heat transfer prediction lacks physical meaning. More research then focused on how to describe the degree of thermal non-equilibrium.

* Corresponding author.
E-mail addresses: zihan.xia@kit.edu (Z. Xia), xu.cheng@kit.edu (X. Cheng).

https://doi.org/10.1016/j.ijheatmasstransfer.2025.127035
Received 3 January 2025; Received in revised form 23 March 2025; Accepted 26 March 2025
Available online 4 April 2025

Nomenclature

General

A	Surface area (m^2)
a	Coefficient relating the drag effect
b	$\frac{3\rho_v}{2\rho_d+\rho_v}$, refers to the vapor acceleration
c	$\frac{18}{(2\rho_d+\rho_v)d}\sqrt{\frac{\rho_v\mu}{\pi}}$, account for the effect of deviation in flow pattern from steady state
b_0	A value determined by energy balance
b_1	Constant for the radial profile of dimensionless velocity
Bo	Boiling number
C	Droplet concentration (kg/ m^3)
C_D	Drag coefficient
c_{ow}	Constant
c_p	Heat capacity (J/kg·K)
c_{ofu}	Coefficient for vapor velocity profile
d	Droplet diameter (m)
D_t	Tube diameter (m)
f	Constant with the default value of 0.4
G	Mass flux, (kg/ m^2·s)
h	Heat transfer coefficient (w/ m^2·K)
K_{vd}	correction factor (0,1)
k_Θ	=0.41, Von Karman constant
L	Heated length(m)
L_{atent}	Latent heat (J/kg)
m_d	Droplet mass flow rate (kg/s)
m_{dep}	Droplet deposition mass flow rate (kg/s)
n_d	Droplet number per volume (/m^3)
Nu	Nusselt number
Pr	Prandtl number
Q	Heat power (W)
q''	Heat flux (W/m^2)
r	Distance to the centerline of tube (m)
r_0	Radius of tube (m)
Re	Reynolds number
Re_d	Relative Reynolds number
S	Slip ratio, u_v/u_d
T	Temperature (K)
T^+	Dimensionless temperature, $T^+ = \frac{T_v-T_w}{T^*}$, $T^* = -\frac{q''_w}{\rho c_p u^*}$
ΔT_w	Wall superheating, $T_w - T_s$
u^*	Shear velocity (m/s)
u^+	Dimensionless velocity, $u^+ = \frac{u_v}{u^*}$
u	Time-average velocity in streamline direction (m/s)
v'	Fluctuation velocity in radial direction (m/s)
v'^+	v'/u^*, dimensionless fluctuation velocity in radial direction
x	Steam quality
y	Distance from wall (m)
y^+	Dimensionless distance from wall, $y^+ = y\cdot\frac{u^*}{\mu_v/\rho_v}$
Δz	Elevation change during two iterations (m)

Greek symbols

α	Void fraction
ε	Turbulent diffusivity (m^2/s)
η_e	The ratio of fluctuation amplitude of the droplet to that of the vapor in the turbulent core
λ	Thermal conductivity (W/m-K)
μ	Dynamic viscosity (Pa-s)
ρ	Density (kg/m^3)

Subscripts

0	Value before iteration
1	Value after iteration
a	Actual value
c	Central region
$c-n$	From central region to near-wall region
cr	Separation between central region and near wall region
cw	Separation between wall boundary region and transition region
d	Droplet
dep	Deposition
dev	Developing post-dryout region
do	Dryout
e	Equilibrium
in	inlet
n	Near wall region
nt	Transition region
nw	Wall boundary region
s	Saturation
t	tube
tr	Transition between regions
v	Vapor
vb	Vapor at the bulk temperature
vc	Vapor at the central region
vd	Vapor to droplet
vn	Vapor at the near wall region
vs	Vapor at saturation temperature
vw	Vapor at the wall temperature
vwb	Vapor at average temperature of wall and bulk vapor temperature
w	Wall
wv	Wall to Vapor
y^+	Value at the position of y^+

Some empirical or semi-empirical correlations [12], based on parameter analysis and data fitting, have been developed to predict the actual vapor temperature or actual steam quality. For example, Chen et al. [13] derived correlations for actual steam quality by analyzing the process of vapor-droplet interfacial heat transfer and data fitting. Yoder and Rohsenow [14] built a first-order differential equation for the actual steam quality. Later, Varone and Rohsenow [15] improved Yoder's model [14] by correlating the wall vapor convective Nusselt number with experimental data, achieving good predictions. The prediction accuracy of empirical correlations is inherently constrained by the parameter range of the experimental data used for regression analysis. To develop a general model capable of elucidating heat transfer mechanisms and a wider application range, mechanistic models which attempt to figure out the individuals' heat transfer process in the PDO region and simulate each process are developed [16–19]. Several correlations for describing the individual processes are used instead of correlating one convection heat transfer coefficient.

In the PDO region, 6 heat transfer paths between the wall, vapor, and droplets are identified: convective heat transfer from wall to vapor, interfacial heat transfer from vapor to droplets, direct contact heat transfer from wall to droplet, and radiative heat transfer among wall, vapor and droplets. Among these heat transfer processes, the interfacial heat transfer determines the amount of heat that droplets absorb from superheated vapor, which determines the degree of vapor superheating. Due to the unknown of droplet evaporation behaviors, predicting the interfacial heat exchange and vapor superheating in the PDO region remains challenging. Therefore, this study focuses on the improvement of interfacial heat transfer model.

In the PDO models, the interfacial heat transfer per unit volume of flow q_{vd} is calculated by:

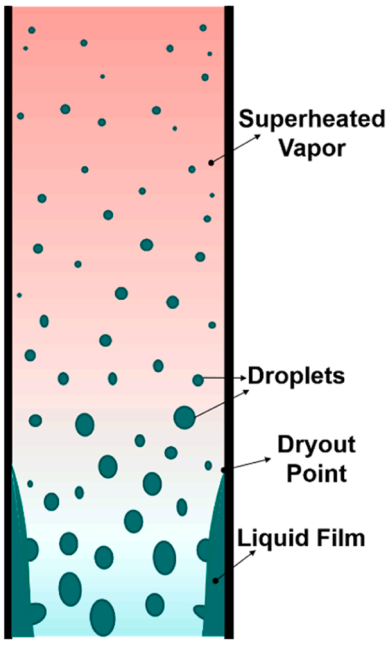

Fig. 1. Schematic of dryout and post-dryout.

$$q_{vd} = h_{vd}(T_v - T_d)n_d\pi d^2 \tag{1a}$$

$$n_d = \frac{6(1-\alpha)}{\frac{\pi}{6}d^3} \tag{1b}$$

Where the interfacial heat transfer coefficient h_{vd} is calculated by the correlations developed from the experiments on single stable droplet evaporation in superheated gas flow [20–22]. $n_d\pi d^2$ refers to the interfacial heat transfer area, which is determined by the total surface area of droplets with size d. n_d is the number of droplets per unit volume, calculated by the droplet void fraction $(1-\alpha)$. Vapor temperature is typically taken as the cross-sectional average vapor temperature by most PDO mechanistic models [17–19] even though the vapor near the wall is probably highly superheated. Specially, in the work of Yu [23], the larger variation of vapor temperature in the radial direction was considered. The flow region was divided into two regions: film region and core region. A film temperature T_{vf} was defined as the average temperature of wall temperature and bulk temperature. The central vapor temperature T_{vc} was defined as the average temperature of bulk temperature and saturation temperature. The interfacial heat flux between the droplet and vapor was calculated as the sum of the two regions' interfacial heat flux as shown in Eq. (2) and a weighting factor K_{vd} was correlated in Eq. (3) to account for the ratio of droplet evaporation at the film vapor temperature. However, this correlation is highly empirical and cannot describe the physical processes of droplet evaporation and droplet lateral movement.

$$\boldsymbol{q}''_{\boldsymbol{vd}} = \boldsymbol{K_{vd}h_{vd,f}}\left(\boldsymbol{T_{vf}} - \boldsymbol{T_d}\right) + (1 - \boldsymbol{K_{vd}})\boldsymbol{h_{vd,c}}(\boldsymbol{T_{vc}} - \boldsymbol{T_d}) \tag{2}$$

$$\boldsymbol{K_{vd}} = 4500\boldsymbol{\alpha_v^2}\left(\frac{\boldsymbol{Re_d}}{\boldsymbol{Re_{vb}}}\right)^{1.5}\left(\frac{\boldsymbol{D_t}}{\boldsymbol{d}}\right)(\boldsymbol{x_e} - \boldsymbol{x_{do}})^2 \tag{3}$$

In the work of Meholic [24], the radial distribution of vapor temperature profile was considered while the changes in this temperature profile due to droplet evaporation were not accounted for. Therefore, the phenomenon of droplet evaporation under high variation of vapor temperature needs more detailed modelling and investigation.

In turbulent flow, droplets exhibit lateral movement, moving from the main flow to the near wall region. The high degree of wall superheating in the PDO region brings a larger difference in vapor temperature between the tube center and the near wall region. Thus, the amount of droplets moving to the near wall region affects the total amount of droplet evaporation [25]. In previous post-dryout heat transfer models, droplet lateral movement was only considered in the calculation of heat transfer between droplets and the wall, with no regard for its impact on interfacial heat transfer [17,18]. Additionally, droplet deposition velocity was typically used to estimate the number of droplets reaching the wall when considering droplet lateral movement. However, previous computational fluid dynamics (CFD) simulations have shown that higher wall temperature leads to an increased droplet evaporation rate in the near wall region [25], which is expected to prevent the droplet moving towards the wall [19]. Despite this, prior models still rely on empirical deposition velocity correlations derived from experiments on unheated surfaces [26–28], thus neglecting the effect of droplet evaporation on deposition velocity. One reason for this limitation is the difficulty of experimental measuring of droplet deposition on heated surfaces under evaporation conditions. Compared to experiments and mechanistic models, CFD can predict the multi-dimensional characteristics of droplets and enabling a deeper understanding of droplet behaviors in the PDO region [29–31]. However, CFD simulation requires substantial computational resources and not suitable for a large number of predictions. Therefore, by integrating the vapor profile and deposition velocity derived from previous CFD simulations [25] into the mechanistic model, a combination of CFD simulation results and one-dimensional mechanistic model can capture the two-dimensional characteristics of droplet evaporation in the PDO region.

This paper introduces an improved post-dryout heat transfer mechanistic model that incorporates a new interfacial heat transfer model, accounts for droplet lateral movement and incorporates the vapor temperature distribution derived from CFD simulation results. The model for droplet deposition is updated to reflect the influence of large droplets in vapor flow and droplet evaporation. Considering the high wall temperature in developed PDO region, droplets can hardly touch and attach to the wall to have efficient heat transfer with the wall [32]. To prioritize improvements in the interfacial heat transfer model while avoiding introducing additional errors, the present PDO heat transfer model neglects direct wall-droplet heat transfer and radiation heat transfer.

2. Model description

Compared to the pre-dryout region, the heated wall in the PDO region is no longer covered by a continuous liquid film. The vapor is continually heated by convective heat transfer from the wall and being superheated. The presence of droplets in the PDO region slows the superheating of vapor as well as the increase in wall temperature. Thus, the interfacial heat transfer process is figured out as the most important part to determine the wall temperature trend after the dryout point. Therefore, the focus of this paper is to develop a new interfacial heat transfer model with better physical meaning.

Investigations on PDO heat transfer and droplet behaviors have been performed with ANSYS FLUENT in the previous studies [25,29]. It was found that over 50 % of droplet evaporation occurs in the near-wall region, which occupies only 25 % of the total flow area. This indicates that the evaporation rate in the near-wall region is nearly three times higher than that in the central region. Given this substantial variation in droplet evaporation across radial positions, the interfacial heat transfer in the mechanistic model should be treated differently from the averaging methods commonly used in the literature. In this study, as shown in Fig. 2, a two-region model is developed by dividing the entire flow region radially into a central region and a near-wall region at r_{cr} to account for the difference in evaporation rate between the two regions. Simulation analysis shows that the high evaporation rate near the wall is primarily due to the elevated vapor temperature in that region. Consequently, the boundary between the central region and the near-wall

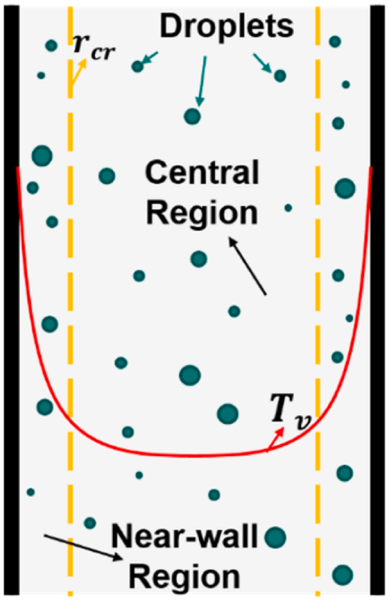

Fig. 2. Schematic of two-region model and vapor temperature profile.

region is defined by the vapor temperature profile T_v. A fitted vapor temperature profile for the PDO region provides s better prediction of interfacial heat transfer in the near-wall region. Additionally, the droplet lateral movement from the central region to the near wall region should be included in the two-region model. Through qualitative and quantitative analysis of the CFD simulation results, the vapor temperature profiles and droplet deposition can be modelled and implemented into the mechanistic model for a more reliable prediction of interfacial heat transfer. The wall temperature then is obtained by employing the wall-vapor convective heat transfer model developed by Yu [23] .

In the current two-region model, the following assumptions are made:

- all droplets are assumed to be spherical, with uniform size and axial velocity in both regions at the same heated length.
- at the dryout point, droplets are assumed to be evenly distributed along the radial direction and at the saturation temperature.
- heat transfer between the droplets and the wall is neglected in this model.

The droplets absorb heat from superheated vapor and evaporate into vapor at the saturated temperature. The newly generated saturated vapor absorbs heat from the superheated vapor and also increases the mass flow rate of vapor flow. Therefore, the proposed two-region model takes into account the changes in vapor temperature and vapor velocity profile due to droplet evaporation. A detailed description of the two-region model for interfacial heat transfer calculation is provided in the following sections.

2.1. Two regions separation

The previous CFD simulations [25,29] employed the Discrete Phase Model in ANSYS FLUENT to simulate the droplet behavior in vapor flow under post-dryout conditions. The droplets are considered as a discrete phase and tracked by Lagrangian approach, while the vapor is considered as a continuous phase. Heat, mass and momentum are transferred between phases. As absorbing heat from the superheated vapor and heated wall, the droplets evaporate into vapor, thereby influencing both the vapor velocity and temperature profiles. This method has been validated for single-phase and two-phase conditions [25]. The relevant droplet parameters were analysed in detail in previous studies [25,29], while the vapor parameters (e.g., temperature and velocity profiles) are used in the current study for model development. In Fig. 3, a typical radial profile of vapor superheating degree $T_{v,sup}$ in the PDO region is represented by the red dotted line. The x-axis is y^+, the dimensionless distance from the wall. The black dashed line represents the superheating degree of the bulk temperature $T_{b,sup}$. A high temperature gradient is observed across the radial direction. The vapor superheating drops sharply from the wall to the position of $y^+ = 300$, marked by the green dashed line. In this region, the vapor temperature significantly exceeds the bulk temperature. Beyond $y^+ = 300$, the vapor is less superheated and varies only slightly as y^+. Therefore, considering that using bulk temperature to calculate interfacial heat transfer fails to capture the near-wall effects, the flow region is divided into a near-wall region and a central region at $y^+ = 300$. The interfacial heat transfer is calculated separately within these two regions. Sensitivity analysis indicates that the predicted wall superheating is not sensitive to the selection of the y^+ value.

2.2. Droplet evaporation in two regions

Fig. 4 provides a partially enlarged view of Fig. 2, illustrating how the regions are separated from the top view and how the two-region model calculates droplet evaporation over a distance increment of Δz in the front view. In the front view, the green rectangle encloses the central region, while the two red rectangles represent the near-wall region. The droplets initially enter the central region and the near-wall region with a mass flow rate of $m_{d,c0}$ and $m_{d,n0}$, respectively. During travel over the distance Δz, the droplets evaporate and decrease in size according to the amount of heat they get from the surrounding vapor. The interfacial heat flow rates in the near-wall region $Q_{vd,n}$ and in the central region $Q_{vd,c}$, are calculated separately, each contributing to the reduction of $m_{d,n0}$ and $m_{d,c0}$. The total interfacial heat transfer between the droplets and superheated vapor in this step is represented by the sum of $Q_{vd,c}$ and $Q_{vd,n}$, which contributes to an increase in the actual steam quality x_a and vapor void fraction α. Besides evaporation, there is also droplet transfer from the central region to the near-wall region, which is indicted by blue arrow and m_{dep}, representing the net droplet deposition rate from the central to the near-wall region.

Given the steep gradient in vapor temperature near the wall, this model, unlike Yu's PDO model [23] which employs an average temperature of wall temperature and bulk temperature, fits a correlation for the vapor temperature profile in the PDO region.

From previous CFD results [25,29], a profile of dimensionless vapor temperature T^+ is correlated and showed below:

$$T^+ = Pr_{vw} \cdot y^+, \text{if } y^+ < y^+_{tr} \tag{4}$$

$$\boldsymbol{T^+ = 0.6 \cdot \frac{Pr_{vwb}}{k_\Theta} \cdot \ln(y^+) + b_0, \text{ if } y^+ \geq y^+_{tr}} \tag{5}$$

y^+_{tr} is the intersection point of the Eqs. (4) and (5). Pr_{vw} is the Prandtl

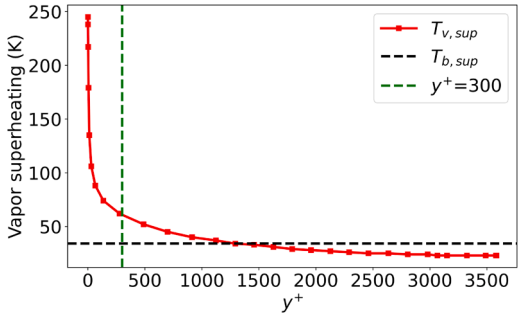

Fig. 3. Profile of vapor temperature in radial direction from CFD simulation [25,29].

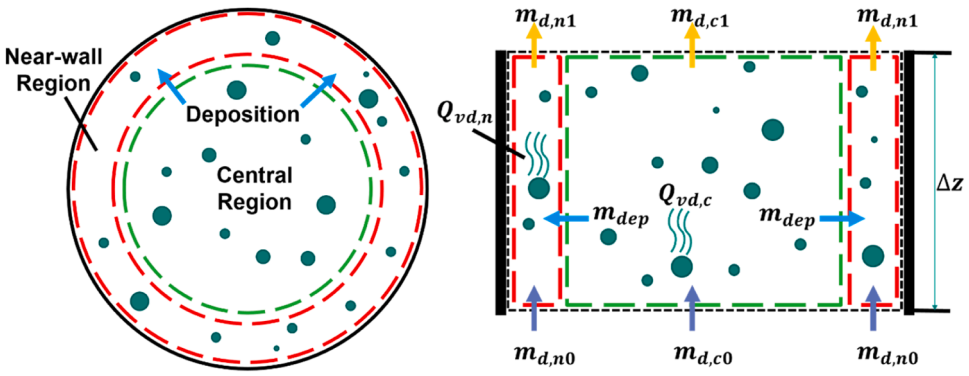

Fig. 4. Evaporation and deposition of droplets in the new two-region model.

number of vapor at the wall temperature T_w. Pr_{vwb} is the Prandtl number of vapor at the average of the wall temperature and the bulk temperature T_{vb}. k_Θ is the Karman constant. The value of b_0 is determined by the energy balance. With this correlation, the vapor temperature in the radial direction can be calculated:

$$T_{v,y} = T_w - \frac{T^+ q_w''}{\rho_v c_{p,v} u^*} \tag{6}$$

Where the q_w'' is the wall heat flux, ρ_v is vapor density, $c_{p,v}$ is vapor capacity, and u^* is friction velocity.

With the vapor temperature known at various radial positions, the near-wall region is laterally discretized into N small slices using logarithmic spacing. In each slice, the vapor temperature is determined and, subsequently, the heat transfer in the near-wall region $Q_{vd,n}$ is calculated. $Q_{vd,c}$ is calculated using the average vapor temperature in the central region, as the temperature gradient is small in this region. According to the Eqn 1a and 1b, the heat transfer to entrained droplets per unit volume of flow channel is calculated by:

$$Q_{vd,\mathrm{n}} = \frac{\sum_{i=0}^{N}(T_{v,\mathrm{i}} - T_s)A_{n,\mathrm{i}} \cdot h_{vd,n} \cdot 6(1-\alpha_n)\Delta z}{d} \tag{7}$$

$$Q_{vd,c} = \frac{(T_{vc} - T_s) \cdot A_c \cdot h_{vd,c} \cdot 6(1-\alpha_c)\Delta z}{d} \tag{8}$$

Where $T_{v,\mathrm{i}}$ and $A_{n,\mathrm{i}}$ refer to the vapor temperature and flow area at the ith slice respectively. $h_{vd,n}$ and $h_{vd,c}$ are the droplet-vapor heat transfer coefficients in the near-wall region and central region, which are calculated separately with their local vapor thermal parameters. T_{vc}, the average vapor temperature in the central region, is obtained from the bulk vapor temperature T_{vb}:

$$T_{vc} = \frac{T_{vb} \cdot A_t - \sum_{i=0}^{N} T_{v,\mathrm{i}} \cdot A_{n,i}}{A_c} \tag{9}$$

The selection of interfacial heat transfer coefficient correlation depends on the range of relative Reynolds number, Re_d:

If $Re_d \le 250$ [20]:

$$h_{vd} = \frac{\left(2 + 0.74 Re_d^{0.5} Pr_v^{\frac{1}{3}}\right) \cdot \lambda_v}{D_t} \tag{10a}$$

If $250 < Re_d \le 450$ [21]:

$$h_{vd} = \frac{\left(2 + 0.6 Re_d^{0.5} Pr_v^{\frac{1}{3}}\right) \cdot \lambda_v}{D_t} \tag{10b}$$

If $Re_d > 450$ [33]:

$$h_{vd} = \frac{\left(2 + 0.27 Re_d^{0.62} Pr_v^{\frac{1}{3}}\right) \cdot \lambda_v}{D_t} \tag{10c}$$

with

$$Re_d = \frac{\rho_v |u_d - u_v| d}{\mu_v} \tag{11}$$

The vapor properties are calculated according to the average vapor temperature of each region. The initial droplet size and droplet velocity are determined by Yoder's model [34] .

According to the definition of the void fraction in Eq. (12), the ratio of liquid fraction can be derived as shown in Eq. (13). The liquid volume fractions in near-wall region $(1-\alpha_n)$ and central region $(1-\alpha_c)$ are obtained by combing Eqs. (13) and (14).

$$\alpha = \frac{1}{1 + S\frac{\rho_v}{\rho_d}\left(\frac{1-x_a}{x_a}\right)} \tag{12}$$

$$\frac{1-\alpha_c}{1-\alpha_n} = \frac{m_{d,c}}{m_{d,\mathrm{n}}} \cdot \frac{u_{d,\mathrm{n}}}{u_{d,c}} \cdot \frac{A_n}{A_c} \tag{13}$$

$$(1-\alpha_n)A_n + (1-\alpha_c)A_c = (1-\alpha)A_t \tag{14}$$

S is the slip ratio and is calculated by [34]:

$$S = \frac{U_v}{U_d} = 1 + 2.31\left[\frac{\rho_d}{\rho_v}\frac{1}{x_a}\frac{q_w''}{GL_{atent}C_D}\frac{d}{D_t}\right]^{0.5} \tag{15}$$

$\frac{u_{d,\mathrm{n}}}{u_{d,c}}$ is the ratio of the droplet axial velocity in the near-wall region ($u_{d,\mathrm{n}}$)

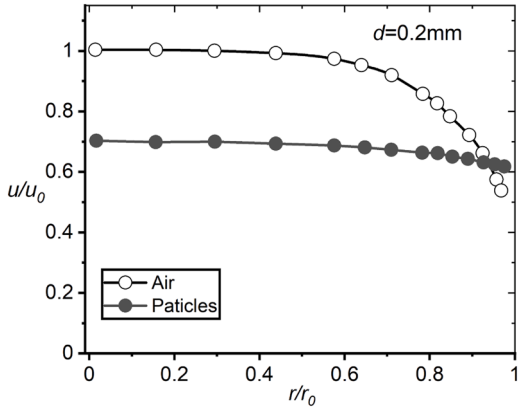

Fig. 5. Streamline velocity of vapor and droplet in Lee (1982) [35].

to that in the central region ($u_{d,c}$). According to Lee's experimental data [35] shown in Fig. 5, the droplet axial velocity changes slightly as approaching to the near-wall region. Therefore, in this paper the droplet axial velocity difference between the two regions is ignored. The liquid fractions in both regions are determined based on the ratio of droplet mass flux in two regions.

After obtaining the values of $Q_{vd,n}$ and $Q_{vd,c}$, the changes in droplet mass flow are iterated across the two regions over the distance of Δz. This allows for the calculation of the mass flow rate at the outlet of the current step, which also serves as the inlet for the next step:

$$m_{d,c1} = m_{d,c0} - m_{dep,c-n} - \frac{Q_{vd,c}}{L_{atent}} \tag{16}$$

$$m_{d,n1} = m_{d,n0} + m_{dep,c-n} - \frac{Q_{vd,n}}{L_{atent}} \tag{17}$$

The amount of droplet deposition between the two regions, $m_{dep,c-n}$, need to be determined and is discussed in the next section. The steam quality at this elevation can be iterated with:

$$x_a = 1 - \frac{m_{d,c1} + m_{d,n1}}{m_{in}} \tag{18}$$

Where m_{in} is the total mass flow rate at the inlet of the test section.

2.3. Droplet deposition between two regions

Previous research on droplet deposition has shown that droplets in the gas tend to move toward the wall. This droplet deposition phenomenon is caused by the radial fluctuation velocity of the gas phase. Fig. 6 presents a schematic of the dimensionless gas fluctuation velocity profile v'^{+}, depicted by a purple line based on the work of Laufer [36]. The radial velocity fluctuation of the vapor increases from the wall to the near-wall region and then slightly decreases as it approaches the tube center. The near-wall region extends from the wall to $y^+_{cr} = 300$, where there is a high gradient of vapor velocity fluctuation. To address droplet lateral movement within this region, the near-wall region is divided into the wall boundary region and the transition region, with $y^+_{cw} = 30$ as the separation line. The wall boundary region and transition region have droplet concentrations C_{nw} and C_{nt} respectively. The droplet concentration in the central region is denoted as C_c. Simulation results from the previous CFD investigation [29] on droplet behavior in the PDO region show that the droplet concentration profile has a V-shaped distribution under turbulent dispersion, as represented by a green line in Fig. 6. In combination with the vapor velocity fluctuation profile, droplets gain momentum and exhibit random motion within the flow due to the stochastic fluctuations of vapor phase. Droplets are distributed radially according to the vapor velocity fluctuation profile. As a result, a concentration valley forms in the transition region following the profile of vapor fluctuation velocity. The droplet lateral movement from the central region to the near-wall region can thus be approximated as being driven by the concentration difference between the central region and the transition region.

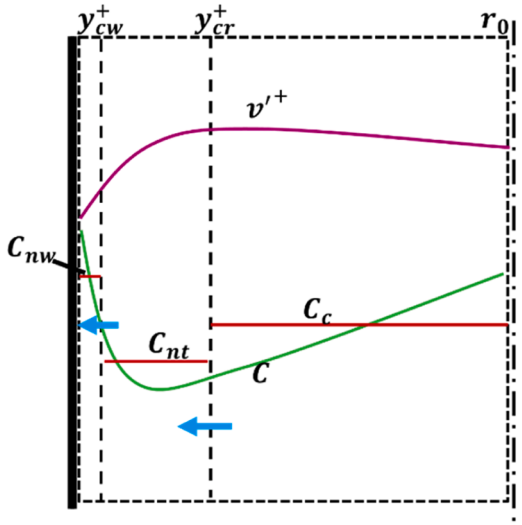

Fig. 6. Profiles of vapor fluctuation velocity and droplet concentration.

The deposition rate from central region to the near-wall region is calculated with particle diffusion equation:

$$m_{dep,c-n} = (D + \varepsilon_d)\frac{dC}{dy}A_{cr} \tag{19}$$

Where ε_d is the droplet turbulent diffusivity, D is the molecular diffusivity, and A_{cr} is the deposition area, representing the surface area of the boundary between the central region and the near-wall region. dy is the distance between the centers of the central region and the near-wall region.

dC is the concentration difference between central region to the transition region, which can be estimated by the difference of C_c and C_{nt}.

The droplet concentrations in the central and near-wall regions are calculated using the void fraction:

$$C_c = (1 - \alpha_c)\cdot\rho_d \tag{20}$$

$$C_n = (1 - \alpha_n)\cdot\rho_d \tag{21}$$

To calculate the net deposition rate, the droplet concentration within the transition region C_{nt} is required.

In Eq. (19), compared to turbulent dispersion [37,38], molecular diffusion is too small to be considered and is therefore ignored. In turbulent flow, the vapor exhibits velocity fluctuations randomly in various directions. Droplets entrained in the turbulent vapor flow are influenced by these fluctuations; however, droplets respond to the vapor fluctuation with a certain delay due to their inertia. The parameter η_e^2 is introduced to quantify the difference between vapor and droplet fluctuations. From Lee [38] and Hinze [39], for short diffusion times, the droplet turbulent diffusivity ε_d can be expressed as:

$$\varepsilon_d = \eta_e^2 \cdot \varepsilon_v \tag{22}$$

Where ε_v is the vapor eddy viscosity and η_e^2 is the fluctuation amplitude ratio of the droplet to that of the vapor in the turbulent core. By obtaining the ε_v and η_e^2, the droplet turbulent diffusivity can be calculated. These two parameters need modifications to fit the PDO conditions.

The following sections detail the calculations of the three unknown parameters, C_{nt}, ε_v and η_e^2, in current deposition model.

Calculation of C_{nt}:

Based on the mechanism of lateral droplet movement near the wall, the droplet concentration within the wall boundary region is governed by the probability of droplets entering versus exiting this region, which is influenced by the disparity in vapor fluctuation velocities between the transition and wall boundary regions. Thus, the droplet concentration ratio c_{ow} between the wall boundary region and the transition region can be quantitatively represented by the ratio of their respective average vapor fluctuation velocities v'_v:

$$\frac{C_{nw}}{C_{nt}} = \frac{v'_{v,nw}}{v'_{v,nt}} = c_{ow} \tag{23}$$

The Laufer's experimental data [36] is displayed in Fig. 7. Beal [40] fitted the experiment data and got correlations below:

$$\frac{v'_v}{u^*} = 0.05y^+ \quad 0 \le y^+ \le 10 \tag{24a}$$

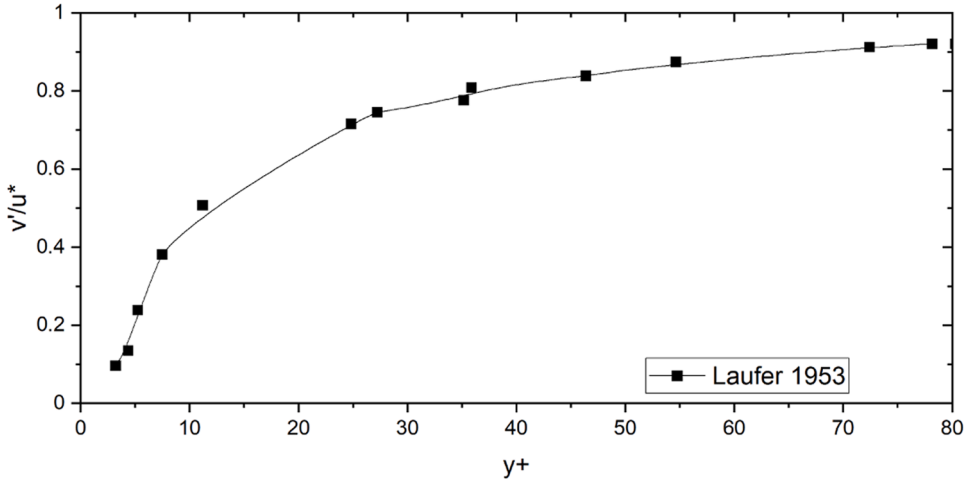

Fig. 7. Profile of dimensionless fluctuation velocity of gas in radial direction.

$$\frac{v'_v}{u^*} = 0.5 + 0.0125(y^+ - 10)\ 10 \le y^+ \le 30 \tag{24b}$$

It should be mentioned that the profile in Eqs. (24a) and (24b) was obtained under single-phase vapor conditions. Under PDO conditions, the presence of droplets and their evaporation in the near-wall region may slightly modify the profile. However, this effect is not considered in the current work. Therefore, the average fluctuation velocity in the wall boundary region and the transition region can be estimated as follows:

$$v'_{v,nw} = 0.48u^* \tag{25a}$$

$$v'_{v,nt} \approx 0.93u^* \tag{25b}$$

$$c_{ow} = 1.9375 \tag{25c}$$

With this ratio the droplet concentration in the transition region can be calculated:

$$C_{nt} = \frac{C_n \cdot A_n}{A_{nt} + c_{ow} \cdot A_{nw}} \tag{26}$$

Calculation of ε_v:

The eddy vicosity of vapor ε_v is considered as not constant across the turbulent core. Kays [41] and Reichardt [42] fitted the radial profile of vapor eddy viscosity as:

$$\varepsilon_v = \frac{k_\Theta r_0 u^*}{6}\left[1 - \left(\frac{r}{r_0}\right)^2\right]\left[1 + 2\left(\frac{r}{r_0}\right)^2\right] \tag{27}$$

r is the radial distance to the tube center, and r_0 is radius of the tube. Eq. (27) is referred by the single phase experiment. To implement it for the dispersed flow, the Eq. (27) need to be modified considering the droplet evaporation effect.

From the work of Reichardt [42], the Eq. (27) is used for generating a profile of dimensionless axial velocity u^+. A relationship between the u^+ and ε_v can be found as:

$$\varepsilon_v = \frac{\mu y_r^+ \, d\left(\frac{r}{r_0}\right)^2}{d(u^+)} \tag{28}$$

y_r^+ is $\frac{ru^*}{\mu/\rho}$. The u^+ correlation for single phase flow is then obtained in Reichardt [42] by the combination of Eq. (27) and (28):

$$u^+ = 2.5\ln\left(y^+ \frac{1.5\left(1 + \frac{r}{r_0}\right)}{1 + 2\left(\frac{r}{r_0}\right)^2}\right) + 5.5 \tag{29}$$

In the PDO region, droplets absorb heat from the vapor and evaporate into vapor, which in turn modifies the vapor velocity profile. Therefore, when the u^+ profile in Eq. (29) is applied to decsribe the velocity profile in the PDO region, it shows a slight difference with the CFD simulated u^+ profile [25,29]. Thus, the u^+ correlation is modified to better represent two-phase flow conditions, based on the CFD-simulated vapor velocity profile from [25,29], as given in Equations (30):

$$u^+ = 2.5 \cdot c_{ofu} \cdot \ln\left(y^+ \frac{1.5\left(1 + \frac{r}{r_0}\right)}{1 + 2\left(\frac{r}{r_0}\right)^2}\right) + b_1 \tag{30a}$$

$$c_{ofu} = 0.88 Pr_{vwb}^{0.3} Pr_s^{0.1} \tag{30b}$$

The c_{ofu} accounts for the effect from droplet evaporation on the vapor velocity profile. It is related to the vapor Prandtl number at the saturation temperature Pr_s and the average of the wall and bulk temperatures Pr_{vwb}. Therefore, from Eqn 28 and 30a, the ε_v in PDO region, accounting for the droplet evaporation effect can be rewritten as:

$$\varepsilon_v = \frac{k_\Theta r_0 u^*}{6 \cdot c_{ofu}}\left[1 - \left(\frac{r}{r_0}\right)^2\right]\left[1 + 2\left(\frac{r}{r_0}\right)^2\right] \tag{31}$$

Calculation of η_e^2

The parameter η_e^2 represents the lag effect of droplet motion relative to vapor fluctuation. For smaller particles, which are light enough to be carried by the continuous flow, $\eta_e^2 \approx 1$. However, droplets are larger in size and cannot follow the turbulent components of the vapor. Therefore, to accurately describe droplet motion in the PDO region, the η_e^2 needs to be modified to consider the relative displacement between the droplets and the vapor phase.

The calculation of η_e^2 is based on the turbulence analysis by Hinze [39]:

$$\eta_e^2 = [1 + f_1(\omega_e)]^2 + f_2^2(\omega_e) \tag{32}$$

Where

$$f_1(\omega_e) = \frac{\omega_e\left(\omega_e + c\sqrt{\frac{\pi\omega_e}{2}}\right)(b-1)}{\left(a + c\sqrt{\frac{\pi\omega_e}{2}}\right)^2 + \left(\omega_e + c\sqrt{\frac{\pi\omega_e}{2}}\right)^2} \tag{33a}$$

$$f_2(\omega_e) = \frac{\omega_e\left(a + c\sqrt{\frac{\pi\omega_e}{2}}\right)(b-1)}{\left(a + c\sqrt{\frac{\pi\omega_e}{2}}\right)^2 + \left(\omega_e + c\sqrt{\frac{\pi\omega_e}{2}}\right)^2} \tag{33b}$$

The ω_e is the most energetic frequency of fluid oscillation [43]:

$$\omega_e = 67.6Re^{0.43} \tag{34}$$

a represents the interfacial drag effect. b refers to the vapor acceleration effect. c accounts for the effect of deviation in the flow pattern from steady state.

In the previous model of Hinze [39], a was calculated according to Stoke's law:

$$a = \frac{36\mu}{(2\rho_d + \rho_v)d^2} \tag{35}$$

But the droplets are larger in size compared to solid particle. Here, a drag force considering the spherical drag law is included. Eq. (35) can be rewritten as:

$$a = \frac{36\mu}{(2\rho_d + \rho_v)d^2\tau} \tag{36}$$

Where

$$\tau = \frac{24}{C_D Re_d} \tag{37}$$

C_D is the drag coefficient. Previously, the $C_D = 24/Re_d$, which means $\tau = 1$. In the proposed model, the C_D is calculated using the correlations developed from Morsi and Alexander [44], the same as the model used in previous CFD simulation [25]:

$$C_D = a_1 + \frac{a_2}{Re_d} + \frac{a_3}{Re_d^2} \tag{38}$$

The value of a_1, a_2, a_3 change with the range of Re_d [44].

With the obtained C_{nt}, η_e^2 and ε_v, Eqn 19 for calculating droplet deposition mass flow rate in the PDO region is rewritten as:

$$m_{dep,c-n} = \eta_e^2 \frac{k_\Theta r_0 u^*}{6 \cdot c_{ofu}} \left[1 - \left(\frac{r}{r_0}\right)^2\right]\left[1 + 2\left(\frac{r}{r_0}\right)^2\right]\frac{dC}{dy}A_{cr} \tag{39}$$

Among them,

$$r = r_{cr} \tag{40a}$$

$$dC = 2(C_c - C_{nt}) \tag{40b}$$

$$dy = \frac{r_{cr} + r_0}{2} \tag{40c}$$

$$A_{cr} = 2\pi r_{cr}\Delta z \tag{40d}$$

Where the r_{cr} is the radial position marking the boundary between the near-wall region and the central region, corresponding to $y^+ = 300$.

3. Model assessment and discussion

In this section, the proposed model is assessed with KIT R-134a PDO experimental data [4,5] and KTH water PDO experimental data [2]. The experimental data points with void fraction at the dryout point over 80 % are selected from the database and used for the model assessment. The predicted wall superheating by the proposed model is compared with the experimental data. The calculated heat transfer coefficient (*htc*) is compared with existing models from the literature. The profile of the predicted wall superheat is analysed using intermediate parameters obtained during the prediction.

3.1. Assessed with KIT R-134a experimental data

The database used for the model assessment comes from Karlsruhe Institute of Technology (KIT) Model Fluid Facility (KIMOF). The refrigerant R-134a flows upward through a vertical round tube. This tube is uniformly heated and has an internal diameter of 10 mm and a heated length of 3000 mm. Detailed information about the test section can be found in the work of Köckert et al. [4] and Rensch et al. [5]. A total of 4760 data points are selected based on the criterion of a dryout void fraction greater than 80 %. Here are the parameter ranges of the selected KIT R-134a experiment parameters:

Working Fluid:	R-134a
Heated Length:	3000 mm
Tube Inner Diameter:	10 mm
Pressure Range:	1.10 – 3.25 MPa
Mass Flux:	300 – 1500 kg/(m^2 · s)
Heat Flux	20 – 140 kW/m^2

3.1.1. Assessment with wall temperature

In Fig. 8, the scatter plot compares the wall superheating predicted by the proposed model with experimentally measured values, based on the 4760 data points from KIT R-134a. It can be observed that significant deviations between predicted and measured wall superheating predominantly occur in regions close to the dryout point. A detailed error analysis of all data points reveals that the majority of points with larger deviations fall within 0.2 m downstream of the dryout location. This corresponds to the period of wall temperature jumping, where the flow has not yet stabilized into a dispersed flow, referred to as the developing PDO region. According to the experimental work of Morse et al. [45], in this region, the base film ruptures due to continuous evaporation and entrainment, temporarily exposing sections of the heated surface to vapor, leading to localized temperature increases. However, as disturbance waves propagate downstream, they intermittently rewet these dry areas, resulting in a fluctuating wet-dry surface condition. Due to the periodic wetting and drying induced by disturbance waves, the measured wall temperature oscillates. The final recorded wall temperature from experiment represents the time-averaged value over a certain period. Therefore, the wall temperature in the developing region depends on the frequency of the disturbance waves and dry fraction. The flow regime in the developing PDO region is a transition between annular flow and dispersed flow [45]. Since the proposed model is

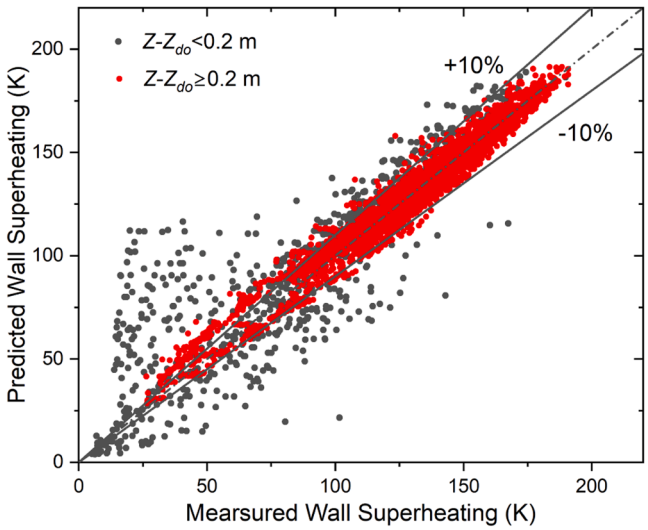

Fig. 8. Comparison of predicted wall superheating and KIT R-134a measured wall superheating.

developed for fully developed post-dryout heat transfer, all points within 0.2 m downstream of the dryout location are marked with black dots. It can be observed that the majority of predictions with errors exceeding the ±10 % margin correspond to these points in black dots. The red dots in Fig. 8 refer to the points fall within the developed PDO region. Approximately 92 % of the 3821 red data points in the developed PDO region fall within the ±10 % error range. This indicates the high reliability of the model in predicting heat transfer in the developed PDO region.

3.1.2. Analysis with heat transfer correlations

Four models from the literature, i.e. Groeneveld equilibrium correlation [9], Chen non-equilibrium correlation [13], Rohsenow non-equilibrium differential model [14], and Yu non-equilibrium mechanistic model [23], are selected for comparison with the proposed model. To quantitatively evaluate the predictive performance of these models, the heat transfer coefficient *htc* is defined with Eq. (41):

$$htc = \frac{q''_w}{T_w - T_s} \tag{41}$$

For each data point, the error parameter is defined by:

$$error(i) = \frac{htc_{cal}(i) - htc_{exp}(i)}{htc_{exp}(i)} \tag{42}$$

Where $htc_{cal}(i)$ is the predicted heat transfer coefficient of the ith point, calculated with the predicted wall temperature. $htc_{exp}(i)$ is the measured heat transfer coefficient, calculated by the measured wall temperature. Moreover, the mean error (ME) and root-mean-square value (RMS) of the error parameter are calculated by:

$$ME = \frac{1}{n}\sum_{i=1}^{n} error(i) \tag{43}$$

$$RMS = \sqrt{\frac{1}{n}\sum_{i=1}^{n} error(i)^2} \tag{44}$$

Accordingly, Table 1 presents the prediction errors of the proposed model and the four selected models from the literature against the KIT R-134a experimental database. As can be seen, the Yu [23] mechanistic model, as well as the proposed mechanistic model, performs better compared to other correlations. The proposed model, with a mean error of −0.6 % and an RMS of 18.87 %, achieves the best prediction accuracy among the four selected models. The comparison with models from the literature demonstrates an obvious improvement in proposed model.

3.1.3. Parameter analysis

In the PDO region, the wall temperature profiles exhibit two possible trends: increasing or decreasing with steam quality increase. Fig. 9 illustrates the wall superheating profiles at mass flux of 300 kg/m^{2}s and a pressure of 2.8 MPa, which displays an increase in wall superheating as heated length increases. Although the proposed model slightly underestimates the wall temperature, it accurately captures the temperature profile at low mass flux and also the effect of heat flux: higher heat flux results in larger wall temperature jumps and an increased maximum wall temperature in PDO region.

Table 1
Assessment of various models of PDO heat transfer based KIT R-134a experimental data.

	ME %	RM S%
Proposed model	−0.6	18.87
Yu model [23]	4.39	24.35
Groeneveld model [9]	17.22	44.13
Chen model [13]	−25.00	48.39
Rohsenow model [14]	41.20	52.91

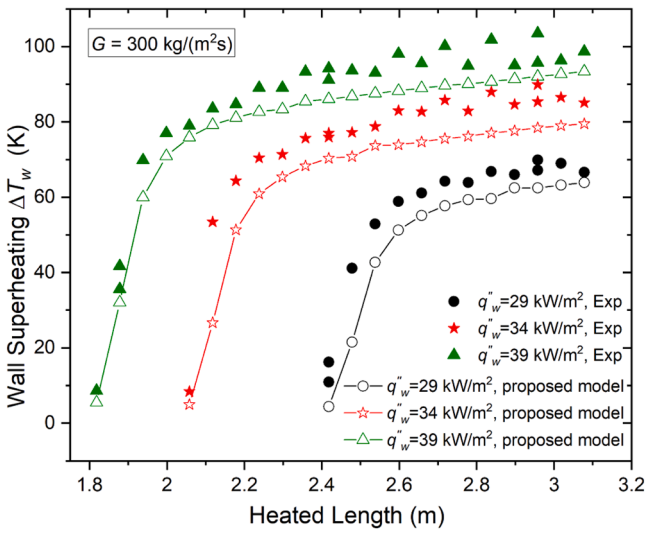

Fig. 9. Wall superheating comparison between the proposed model and experimental data at low mass flux of pressure 2.8 MPa.

The predicted bulk vapor superheating at different heat flux is plotted against the dimensionless distance from dryout point, represented by the difference between equilibrium quality x_e and the steam quality at dryout point x_{do} in Fig. 10. Since the proposed model assumes thermal equilibrium condition at dryout, the vapor superheating starts from 0 and increases as the heated length increases. It can be seen that cases with different heat fluxes have similar profiles of vapor superheating. At the end of the heated length, the vapor superheating reaches its maximum value of 30 K.

The predicted heat transfer coefficients by proposed model, htc_{vb}, are calculated according to Eq. (45) to illustrate the variation of convective heat transfer under different conditions.

$$htc_{vb} = \frac{q''_w}{T_{w,cal} - T_{vb}} \tag{45}$$

Where $T_{w,cal}$ and T_{vb} are predicted wall temperature and bulk temperature predicted by the proposed model. In Fig. 11, it can be seen that the three cases under different heat flux have close profiles of htc_{vb}. The htc_{vb} has an increasing trend in developed PDO region since the droplet evaporation increases the vapor mass flux, enhancing the wall vapor

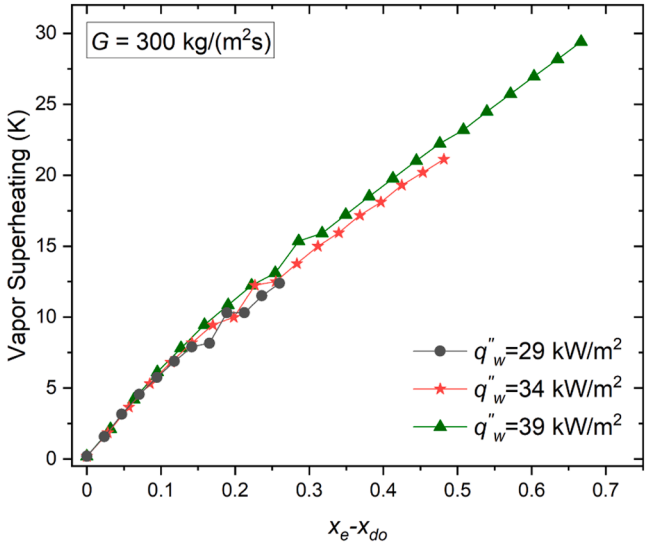

Fig. 10. The predicted bulk vapor superheating under low mass flux.

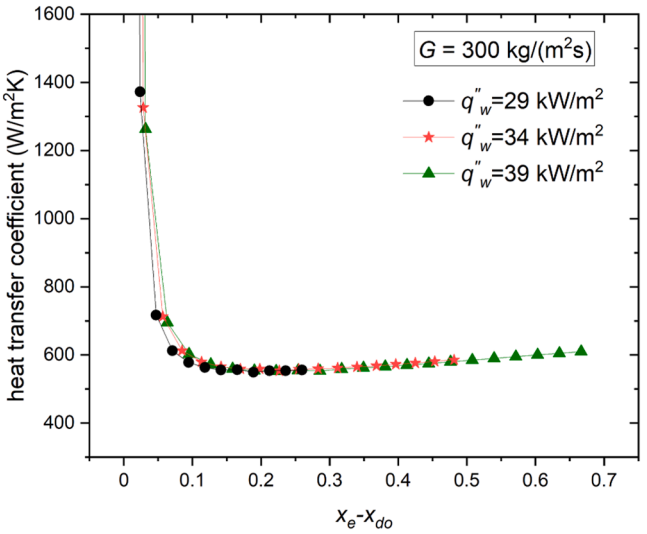

Fig. 11. The predicted heat transfer coefficient htc_{vb} under low mass flux.

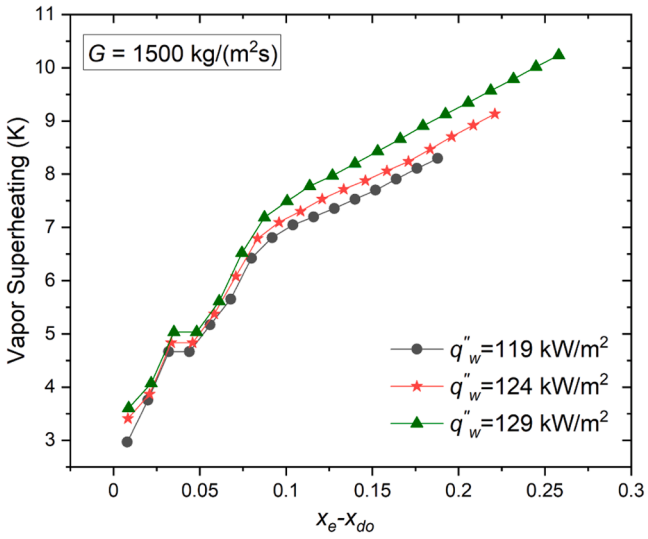

Fig. 13. The predicted bulk vapor superheating under high mass flux.

convective heat transfer. However, since the degree of vapor superheating continuously increases at a relatively large rate, the effect of vapor superheating is stronger than the enhancement on convective heat transfer. Consequently, wall superheating steadily rises in the PDO region.

Fig. 12 presents the wall superheating profiles for a high mass flux of 1500 kg/m²s at 1.1 MPa, where a decrease in wall temperature occurs in the developed PDO region. The proposed model effectively reproduces this behavior.

Fig. 13 displays the predicted vapor superheating under high mass flux. Under these conditions, the vapor superheating profiles for different heat fluxes exhibit similar trends. The rate of increase in vapor superheating is slower and smaller compared to that at low mass fluxes. The heat transfer coefficients htc_{vb} under high mass flux for three different heat fluxes are also displayed in Fig. 14. The profile of htc_{vb} demonstrate an initial decline, followed by a significant increase in the developed PDO region. Since the enhancement in the heat transfer coefficient outweighs the effect of the slowly rising vapor superheating, the wall temperature decreases under high mass fluxes.

The analysis of the results at different mass fluxes and heat fluxes reveals that variations in heat flux do not significantly affect the heat

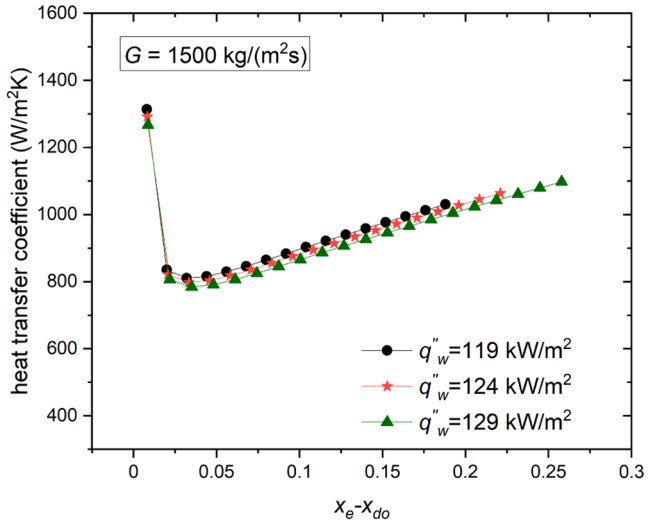

Fig. 14. The predicted heat transfer coefficient htc_{vb} under high mass flux.

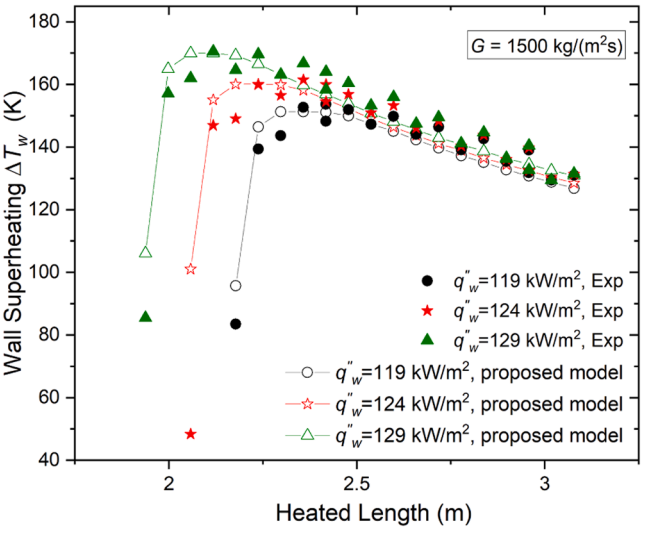

Fig. 12. Wall superheating comparison between the proposed model and experimental data at high mass flux of pressure 1.1 MPa.

transfer pattern in the proposed model. Instead, mass flux is the primary factor influencing the wall temperature trend in the PDO region. To minimize the impact of other parameter variations, results obtained for three mass fluxes at the same pressure and similar heat flux are selected for further analysis. Fig. 15 presents the profiles of wall superheating at a pressure of 1.6 MPa (reduced pressure of 0.4) for various mass fluxes. The proposed model captures the trend of PDO wall superheating well in different mass fluxes.

To understand the difference in wall superheating profiles predicted by the proposed model, the vapor temperature and interfacial heat transfer are displayed in Fig. 16 and Fig. 17. Fig. 16 indicates that the rates of increase in vapor superheating under different mass fluxes vary significantly. At low mass flux, the maximum bulk vapor superheat reaches 30 K, while at high mass flux, it is only 5 K. This difference in vapor superheating can be explained in Fig. 17, which displays the ratio of total interfacial heat transfer power Q_{vd} to total heat power from the heated wall Q_w. It shows that the proportion of interfacial heat transfer under different mass fluxes varies significantly. At low mass flux, the interfacial heat transfer proportion is only about 40 %, while at high mass flux, it approaches nearly 100 %. Analysis of intermediate parameters reveals that the disparity in interfacial heat transfer is

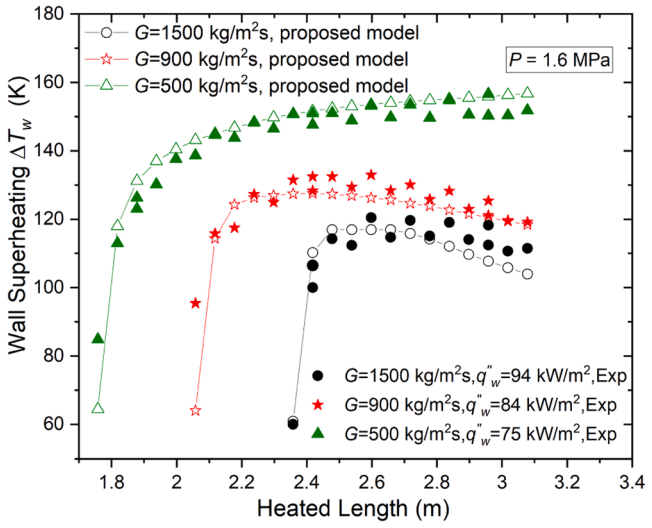

Fig. 15. Wall superheating comparison between proposed model and experimental data under various mass fluxes.

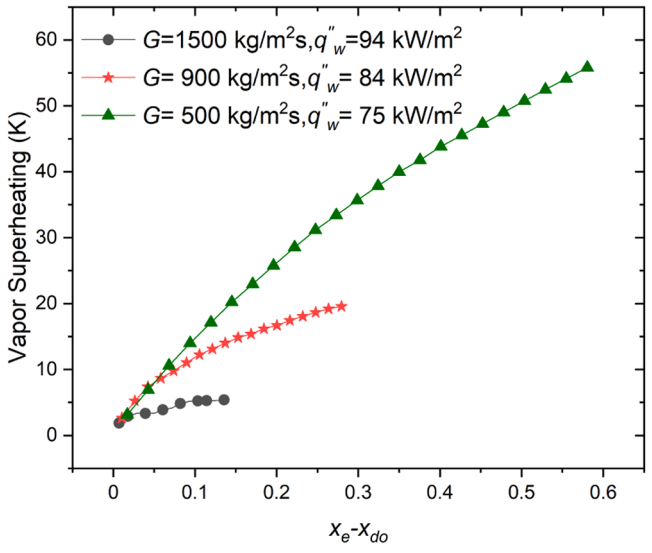

Fig. 16. The predicted bulk vapor superheating under various mass fluxes.

primarily due to the higher x_{do} and the smaller droplet size caused by increased vapor velocity at high mass flux, which leads to a higher droplet interfacial area concentration. Consequently, interfacial heat transfer efficiency is significantly enhanced under high mass flux conditions, resulting in reduced and slower vapor superheating. Additionally, the convective heat transfer under high mass flux is highly efficient due to a higher Reynolds number. As a result, the predicted wall temperature shows a decreasing trend in the developed PDO region.

3.2. Assessed with KTH experimental data in water

The KTH experimental data with water [2] is selected to further evaluate the proposed model. The KTH experiment is conducted in a vertically oriented tube, which is electrically and uniformly heated, with water flowing upwards. A total of 3968 data points, meeting the criterion of a void fraction greater than 80 %, are selected for assessment. Here are the parameter ranges of the selected data points:

Working Fluid:	Water
Heated Length:	7000 mm

(*continued on next column*)

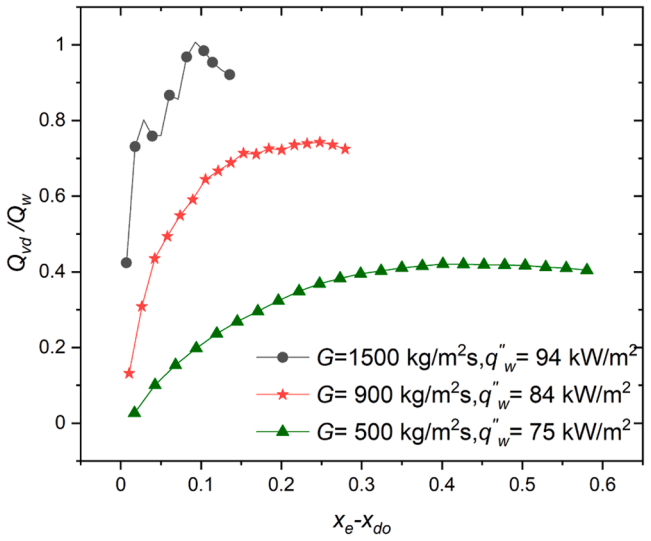

Fig. 17. The predicted ratio of interfacial heat transfer power and total heat power from the wall under various mass fluxes.

(*continued*)

Working Fluid:	Water
Tube Inner Diameter:	14.9 mm, 10 mm
Pressure Range:	3 – 16 MPa
Mass Flux:	500 – 3000 kg/(m^2 · s)
Heat Flux	147 – 1295 kW/m^2

3.2.1. Wall superheating

Fig. 18 presents a comparison of the predicted and measured wall superheating based on KTH water data. To ensure the data represent the fully developed PDO region, 3003 points located >0.5 m away from the dryout points are included. The scatter plot reveals a slightly larger deviation compared to the previous R-134a data. Despite this, approximately 87 % of the data points fall within $a \pm 30$ % error margin, and 71 % fall within $a \pm 20$ % margin, indicating that the model demonstrates reasonable predictive accuracy for the water dataset.

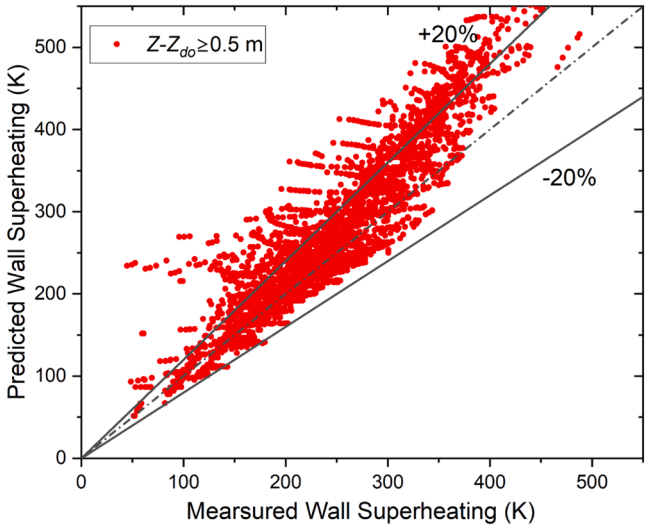

Fig. 18. Comparison of predicted wall superheating with the measured wall superheating.

3.2.2. Analysis with heat transfer coefficient

As the assessment with R-134a data, the prediction errors for the heat transfer coefficient in the water dataset are calculated according to Eqn 41 -) and compared with the four selected models, as summarized in Table 2. Among these models, Rohsenow's model [15] demonstrates the smallest mean error of −3.91 % and a relatively small RMS error of 29.07 %. However, considering its poor performance with the R-134a experimental data, its better performance with the water dataset may be attributed to their Nusselt correlation, which is correlated by water and Freon-12 experimental data. In contrast, the proposed model still performs well in water dataset by yielding the smallest RMS error. This suggests that, while the proposed model generally underpredicts the water PDO experimental data, it exhibits minimal error dispersion. This is also illustrated in Fig. 18, where the data points lie slightly above the diagonal line, indicating a slight underestimation of the heat transfer coefficient.

3.2.3. Parameter analysis

Fig. 19 and Fig. 20 present the profiles of wall superheating for water at different heat fluxes under low and high mass fluxes, respectively. Consistent with the trends observed for R-134a in Fig. 9 and Fig. 12, the wall superheating in water exhibits a gradual increase at low mass fluxes and a reduced slope under high mass fluxes in the developed PDO region. Differently, wall superheating in the PDO region for water is significantly higher than that observed for R-134a. In Fig. 19, the predicted profile of wall superheating aligns closely with the experimental results at different heat fluxes under low mass flux. Despite localized deviations as heat flux increases, the overall trend of the wall superheating profile is well captured. Fig. 20 shows the wall superheating profile at high mass flux under different heat fluxes. Although the model slightly overpredicts the wall superheating, it successfully captures the decreasing trend of wall superheating at high mass fluxes. These results demonstrate that the model effectively predicts the wall superheating trends of water under both low and high mass flux conditions.

The actual vapor superheating and the interfacial heat transfer for water cases are also analysed. As shown in Fig. 21, the vapor superheating increases linearly with equilibrium steam quality at low mass flux, reaching up to 60 K. However, in Fig. 22, the vapor superheating at high mass flux initially rises more steeply due to the sharp jump in wall temperature. In the developed PDO region, the increase in vapor superheating becomes less pronounced.

Analysis of interfacial heat transfer in Fig. 23 and Fig. 24 reveals that, at high mass fluxes, the proportion of interfacial heat transfer rapidly increases from zero to a dominant value, stabilizing at approximately 90 %. Conversely, at low mass fluxes, the proportion of interfacial heat transfer rises more gradually, peaking at around 60 %. As the heated length further increases, droplet consumption reduces the droplet concentration, leading to a slight decrease in the proportion of interfacial heat transfer.

4. Conclusion

The present model introduces a two-region model for describing the process of interfacial heat transfer in PDO region. The following results are obtained from the analyses of post-dryout heat transfer in upward flow within a uniformly heated vertical tube, and its assessment with experimental data obtained in water and R134a:

1. Previous CFD simulations [25,29] have revealed significant radial temperature gradient in the vapor phase, suggesting that using bulk vapor temperature to predict interfacial heat transfer, as in the earlier PDO mechanistic models, is inadequate. To address this limitation, this paper introduces a two-region model that considers the droplet evaporation in central region and near-wall region separately. A radial vapor temperature profile is fitted for interfacial heat transfer calculations. A new approach for counting the droplet lateral movement between the central and near-wall regions is also incorporated.
2. Based on the single-phase correlation from literature and vapor parameters from CFD PDO simulations [25,29], an improved correlation for radial vapor temperature profile is fitted, which can account for the modifications of droplet evaporation on the vapor temperature distribution.
3. Since existing deposition correlations are inadequate for predicting droplet movement from the central region to the near-wall region, a

Table 2
Comparison of the predicted heat transfer coefficient with the KTH experimental data.

	ME %	RM S%
Proposed model	−11.68	27.69
Rohsenow model [15]	−3.91	29.07
Yu model [23]	−13.36	29.68
Chen model [13]	−23.13	51.39
Groeneveld model [9]	58.31	100.16

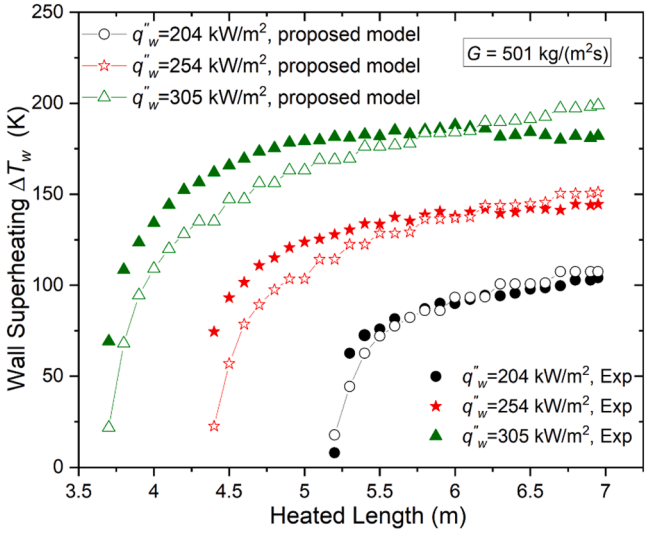

Fig. 19. Comparison of the predicted wall temperature with measured results at low mass flux of pressure 16MPa.

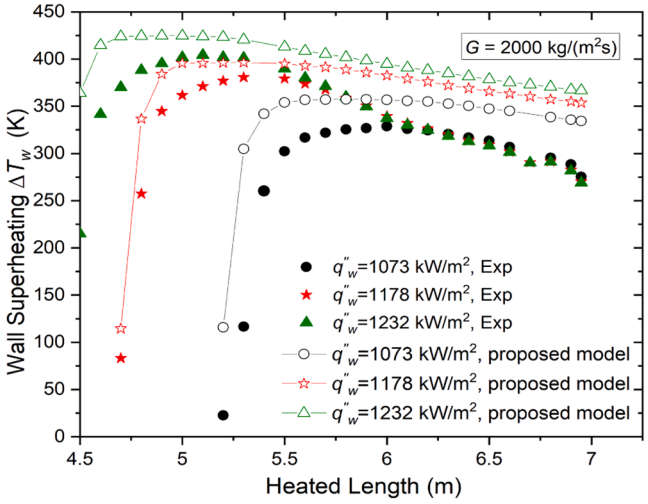

Fig. 20. Comparison of the predicted wall temperature with measured results at high mass flux of pressure 5MPa.

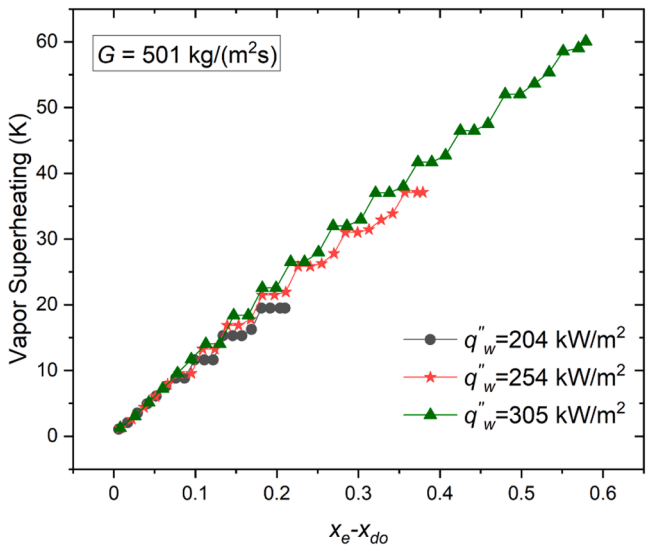

Fig. 21. The predicted bulk vapor superheating under low mass flux.

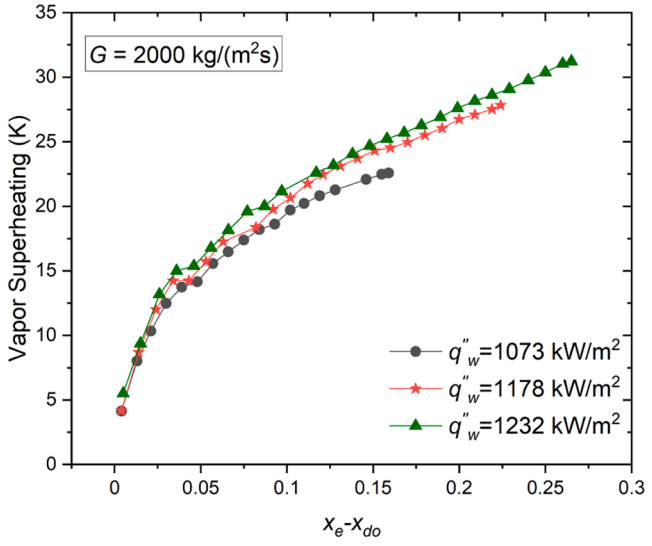

Fig. 22. The predicted bulk vapor superheating under high mass flux.

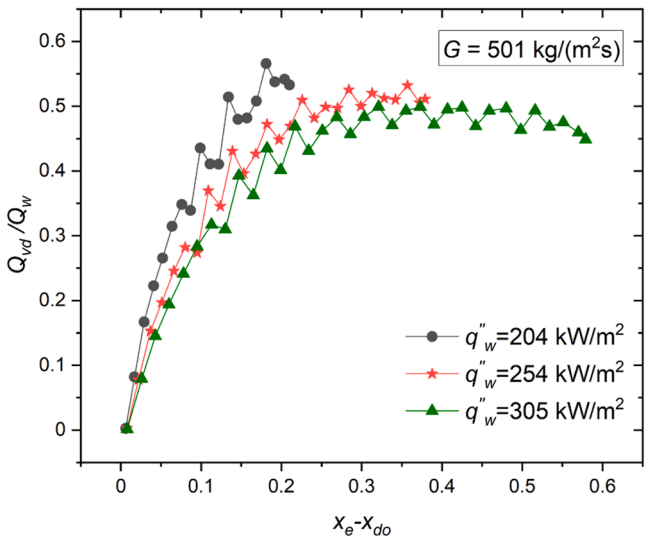

Fig. 23. The predicted ratio of interfacial heat transfer power and total heat power from the wall under low mass flux.

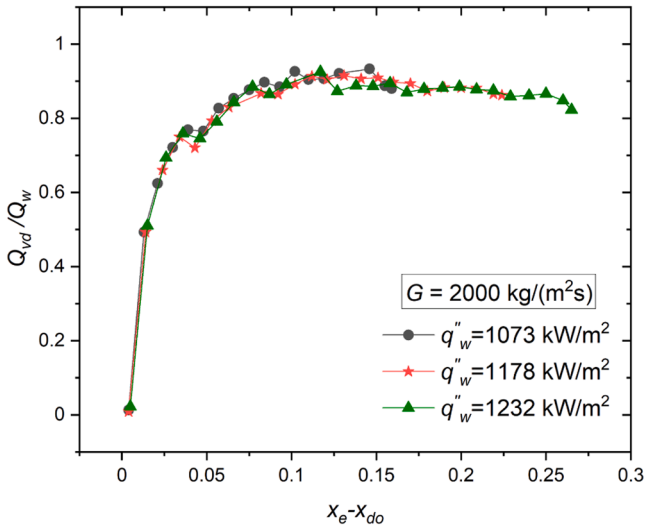

Fig. 24. The predicted ratio of interfacial heat transfer power and total heat power from the wall under high mass flux.

new deposition correlation tailored to the two-region framework is derived. For applicability to post-dryout heat transfer, this correlation is further refined by incorporating vapor velocity profiles fitted from CFD simulations [25,29] and accounting for the drag force on large droplets.

4. Total >8000 data points from KIT R-134a and KTH water data points are selected to assess the proposed model. For R-134a, 92 % of the data points fall within $a \pm 10$ % error margin for wall superheating, while for water, 87 % of the data points fall within $a \pm 30$ % error margin. Validation against experimental wall temperature data for both fluids demonstrates that the model effectively predicts wall superheating in the developed PDO region across a wide range of operating conditions and working fluids.
5. When comparing the heat transfer coefficient with four existing prediction models from the literature, the proposed model demonstrates significantly improved accuracy for KIT R-134a data and slightly better performance for KTH water data. These results indicate that the present model provides reliable predictions on PDO heat transfer, offering a substantial improvement over existing models.
6. With the present mechanistic model, two different behaviours of wall superheating at different mass fluxes can be well explained. When the effect of increased wall vapor convection outweighs the rise in vapor superheating, the wall superheating exhibits a decreasing trend. Conversely, when the vapor superheating increase dominates, the wall superheating continues to rise.

The proposed model demonstrates the good ability to predict post-dryout heat transfer across a wide range of flow conditions and fluids. However, it underestimates the post-dryout heat transfer in the case of water and requires further investigations. Additionally, considering the sensitivity of post-dryout heat transfer to droplet size, an improved droplet size model that accommodates different fluids and flow conditions needs to be considered. Moreover, in the developing PDO region, where the disturbance wave plays an important role, droplets may fall back to wet the heated wall, leading to efficient heat transfer. To improve the predictive capability for this region, future work will incorporate the mechanism of disturbance wave and wall-droplet contact heat transfer during the intermittent dryout. Furthermore, if the

proposed model is to be extended to conditions with much higher wall temperatures in the future, radiative heat transfer may need to be considered. In such cases, the emissivity must be carefully evaluated.

CRediT authorship contribution statement

Zihan Xia: Writing – original draft, Visualization, Validation, Software, Methodology, Investigation, Formal analysis, Data curation, Conceptualization. **Xu Cheng:** Writing – review & editing, Supervision, Resources, Project administration, Funding acquisition.

Declaration of competing interest

The authors declare that they have no known competing financial interests or personal relationships that could have appeared to influence the work reported in this paper.

Acknowledgements

This work is sponsored by the German Federal Ministry of Education and Research (BMBF) under the contract number 02NUK062A. The partial financial support for the first author through China Scholarship Council (CSC) is highly appreciated. Responsibility for the content of this report lies with the authors.

Data availability

Data will be made available on request.

References

[1] A. Bennett, G. Hewitt, H. Kearsey, R. Keeys, Heat Transfer to Steam-Water Mixtures Flowing in Uniformly Heated Tubes in Which the Critical Heat Flux Has Been Exceeded, Atomic Energy Research Establishment, Harwell, England, 1967. Technical Report REP/AERE-R-5373.
[2] K.M. Becker, C.H. Ling, S. Hedberg, G. Strand, An Experimental Investigation of Post Dryout Heat Transfer, KTH, Stockholm, Sweden, 1983. Report KTH-NEL-33.
[3] A. Era, G. Gaspari, A. Hassid, A. Milani, R. Zavattarelli, Heat transfer data in the liquid deficient region for steam-water mixtures at 70 kg/cm2 flowing in tubular and annular conduits, in: Technical Report No. 11, Centro Informazioni Studi Esperienze, Italy, 1966.
[4] L. Köckert, A.F. Badea, X. Cheng, D. Yu, D. Klingel, Studies on heat transfer in R-134a vertical flow, Int. J. Adv. Nucl. Reactor Des. Technol. 3 (2021) 44–53.
[5] N. Rensch, L. Köckert, A.F. Badea, X. Cheng, Experimental investigation of post-dryout heat transfer with R-134a at high pressures, Nucl. Sci. Eng. October (2024) 1–20.
[6] F. Dittus, L. Boelter, Heat transfer in automobile radiators of the tubular type, Univ. California Publications Eng. 2 (1930) 443–461.
[7] R. Winterton, Where did the dittus and boelter equation come from? Int. J. Heat. Mass Transf. 41 (1998) 809–810.
[8] K.J. Liesch, G. Raemhild, K. Hofmann, Zur bestimmung des Wärmüberganges und der kritischen Heizflächenbelastung im hinblick auf besondere verhältnisse in den Kühlkanälen eines DWR bei schweren kühlmittelverlustunfällen, in: Technical Report MRR 150, Laboratorium für Reaktorregelung und Anlagensicherung, 1975.
[9] D.C. Groeneveld, G.G.J. Delorme, Prediction of thermal non-equilibrium in the post-dryout regime, Nucl. Eng. Des. 36 (1976) 17–26.
[10] I. Vojtek, Auswertung Der 25-Stabbündel-Versuche Mit Dem Rechenprogramm BRUDIVA, Gesellschaft für Anlagen- und Reaktorsicherheit, 1978. Technical Report GRS-A-208.
[11] J.D. Parker, R.J. Grosh, Heat Transfer to a Mist Flow, Argonne National Laboratory Subcontract, 1961. Technical Report ANL-6291.
[12] K. Nishikawa, S. Yoshida, H. Mori, H. Takamatsu, Post-dryout heat transfer to freon in a vertical tube at high subcritical pressures, Int. J. Heat Mass Transfer 29 (8) (1986) 1245–1251.
[13] J.C. Chen, F.T. Ozkaynak, R.K. Sundaram, Vapor heat transfer in postCHF region including the effect of thermodynamic non-equilibrium, Nucl. Eng. Des. 51 (2) (1979) 143–155.
[14] G. Yoder, W. Rohsenow, A solution for dispersed flow heat transfer using equilibrium fluid conditions, J. Heat. Transfer. 105 (1983) 10–17.
[15] A.F. Varone, W.M. Rohsenow, Post dryout heat transfer prediction, Nucl. Eng. Des. 95 (1986) 315–327.
[16] P. Saha, A non-equilibrium heat transfer model for dispersed droplet PostDryout regime, Int. J. Heat Mass Transfer 23 (1980) 483–492.
[17] D. Yu, F. Feuerstein, L. Koeckert, X. Cheng, Analysis and modeling of post-dryout heat transfer in upward vertical flow, Ann. Nucl. Energy 115 (2018) 186–194.
[18] Y. Guo, K. Mishima, A non-equilibrium mechanistic heat transfer model for post-dryout dispersed flow regime, Exp. Therm. Fluid. Sci. 26 (2002) 861–869.
[19] X. Cheng, F. Feuerstein, D. Klingel, D. Yu, Mechanistic prediction of post dryout heat transfer and rewetting, Kerntechnik 83 (3) (2018) 203–207.
[20] W. Ranz, W. Marshall, Evaporation from drops, Chem. Eng. Progress 48 (1952) 141–146.
[21] K. Lee, D. Ryley, The evaporation of water droplets in superheated steam, J. Heat. Transfer. 90 (1968) 445–451.
[22] M. Yuen, L. Chen, Heat-transfer measurements of evaporating liquid droplets, Int. J. Heat. Mass Transf. 21 (1978) 537–542.
[23] D. Yu, Analysis and Modelling of Full-Range Post-Dryout Heat Transfer in Vertical Tubes, Karlsruhe Institute of Technology, 2019. Dissertation.
[24] M. Meholic, The Development of a Non-Equilibrium Dispersed Flow Film Boiling Heat Transfer Modeling Package, The Pennsylvania State University, 2011. Dissertation.
[25] Z. Xia, X. Cheng, Numerical investigation on droplet lateral movement in post-dryout region, Int. J. Heat. Mass Transf. 237 (2025) 126448.
[26] S.K. Friedlander, H.F. Johnstone, Deposition of suspended particles from turbulent gas streams, Ind. Eng. Chem. 49 (1957) 1151–1156.
[27] B.Y. Liu, T.A. Ilori, Aerosol deposition in turbulent pipe flow, Environ. Sci. Technol. 8 (4) (1974) 351–356.
[28] G.A. Sehmel, Aerosol Deposition from Turbulent Airstreams in Vertical conduits, Rep. BNWL-578, Batelle Northwest Lab, Richland, Washington, 1968.
[29] Z. Xia, X. Cheng, W. Liu, CFD simulation on droplet behaviour in post-dryout region, Kerntechnik 89 (2024) 124–132.
[30] W. Fan, H. Li, H. Anglart, A study of rewetting and conjugate heat transfer influence on dryout and post-dryout phenomena with a multi-domain coupled CFD approach, Int. J. Heat. Mass Transf. 163 (2020) 120503.
[31] J. Shi, B. Sun, G. Zhang, F. Song, L. Yang, Prediction of dryout and post-dryout wall temperature at different operating parameters for once-through steam generators, Int. J. Heat. Mass Transf. 103 (2016) 66–76, b.
[32] G. Kendall, W. Rohsenow, Heat Transfer to Impacting Drops and Post Critical Heat Flux Dispersed Flow, Heat Transfer Laboratory, Dept. of Mechanical Engineering, Cambridge, MA, 1978. Technical Report MIT-56987-100.
[33] G.A. Hughmark, Mass and heat transfer from rigid spheres, AIChE Journal 13 (1967) 1219–1221.
[34] G.L. Yoder, W. Rohsenow, Dispersed Flow Film Boiling, Massachusetts Institute of Technology. Heat Transfer Laboratory, 1980. Technical Report 85694-103.
[35] S.L. Lee, F. Durst, On the motion of particles in turbulent duct flows, Int. J. Multiphase Flow 8 (2) (1982) 125–146.
[36] J. Laufer, The Structure of Turbulence in Fully Developed Pipe Flow, NACA 1174, National Advisory Committee for Aeronautics, 1954.
[37] Z.H. Yang, S.L. Lee, On the droplet deposition and mist supercooling in a turbulent channel flow, Part. Part. Syst. Charact. 8 (1991) 72–78.
[38] S.L. Lee, M.A. Wiesler, Theory on transverse migration of particles in a turbulent two-phase suspension due to turbulent diffusion-I, Int. J. Multiphase Flow 13 (1) (1987) 99–111.
[39] J.O. Hinze, Turbulence, 2nd edn., McGraw-Hill, New York, 1959.
[40] S.K. Beal, Deposition of particles in turbulent flow on channel or pipe walls, Nucl. Sci. Eng. 40 (1) (1970) 1–11.
[41] W.M. Kays, Convective Heat and Mass Transfer, McGraw-Hill, New York, 1966.
[42] H. Reichardt, Vollstandige darstellung der Turbulenten geschwindigkeitsverteilung in glatten Leitungen, Zeitschrift für Angewandte Mathematik und Mechanik 31 (1951) 208–219.
[43] S.L. Lee, T. Börner, Fluid flow structure in a dilute turbulent two-phase suspension flow in a vertical pipe, Int. J. Multiphase Flow 13 (2) (1987) 233–246.
[44] S.A. Morsi, A.J. Alexander, An investigation of particle trajectories in two-phase flow systems, J. Fluid. Mech. 55 (1972) 193–208.
[45] R.W. Morse, J. Chan, E.T. Hurlburt, J.-M. Le Corre, A. Berson, G.F. Nellis, K. M. Dressler, A new paradigm for the role of disturbance waves on film dryout and wall heat transfer in annular two-phase flow, Int. J. Heat. Mass Transf. 219 (2024) 124812.